

## 4 Detector performance

---

### 4.1 Introduction

In Chapter 2 we have discussed in detail the technical performance of the RICH. In the following we shall try to demonstrate that given the basic technical performance studied and optimized in single track tests, we are able, in the very dense environment of ALICE, to extract the Cherenkov angle of emission with satisfactory precision. It is important to remember that the range for  $\pi/K$  positive identification of the HMPID is limited to momenta  $\gtrsim 1$  GeV/ $c$  for pions and kaons and even higher for protons (because of the threshold effect for Cherenkov photon emission). In the low magnetic field of ALICE, tracks with these momenta are almost straight so that the maximum angle of incidence is limited to  $\sim 10^\circ$ . This means that most of the patterns will be closed ellipses, a feature that eases the pattern recognition.

In the first part we shall describe the ALICE environment in which the detection will take place. To do so we have simulated the complete response of the ALICE experiment including the material budget of all detectors, using the GEANT and FLUKA packages, and an event generator which produces the highest rapidity density expected in Pb–Pb collisions, i.e. 8000 charged particles per unit of rapidity. By applying a detailed simulation of the RICH response, described in Chapter 2, we can then generate the pad map of hits on the RICH modules. This simulation gives an upper limit on the occupancy we can expect and therefore sets the requirements for the pattern recognition performance described afterwards.

In the second part we describe a pattern recognition algorithm that allows to extract the Cherenkov signal in the conditions of occupancy as generated by the simulations.

In the third part we shall describe the matching of tracks from the TPC to the HMPID. The pattern recognition depends critically on the capability to track particles through the tracking detectors of ALICE — the Inner Tracker System (ITS) and the Time Projection Chamber (TPC) — and to extrapolate the tracks, with sufficient precision up to the HMPID (more than two metres away).

In the fourth part we review further work on the optimization of the design, using the described tools of simulation, tracking and pattern recognition.

All the results presented in this chapter have been obtained, using the tracking precision and the material budget quoted in the ALICE Technical Proposal [1].

### 4.2 Simulation of the RICH response in the ALICE radiation environment

#### 4.2.1 Particle multiplicities at the HMPID and secondary interactions

The detector modules will be installed at a radius of 4.8 m and will cover one unit of rapidity with a 16% coverage in azimuth.

For the highest anticipated charged particle multiplicities of 8000 particles per unit of rapidity in central Pb–Pb collisions at  $\sqrt{s} = 5.5$  TeV/nucleon, the predicted densities of charged pions and kaons with momenta above 1 GeV/ $c$  (signal particles) is  $\sim 5$  m<sup>-2</sup> at the position of the RICH. The flux of lower-momentum primary particles and secondary particles produced in detector elements below the RICH and in structural elements like the front absorber, the vacuum chamber and support structures is of the order of 100 m<sup>-2</sup>. These particles have, in general, a much larger angle of incidence than those concerned by the HMPID ( $p \gtrsim 1$  GeV/ $c$ ), which have  $\theta_{\text{in}} \leq 10^\circ$ . The distribution of the angles of incidence as a function of the particle momenta is shown in Fig. 4.1.

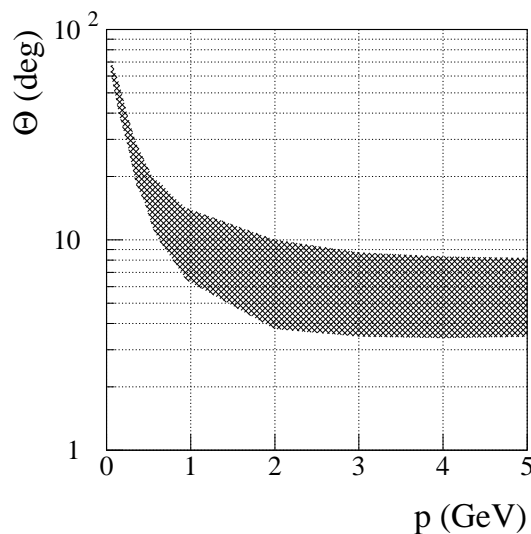


**Figure 4.1:** Variation of the primary particles angle of incidence in function of momentum. The band represents the  $1\sigma$  spread in angle at a given momentum.

The radiation and hadronic interaction lengths of the RICH radiator (vessel material + liquid) is 13% and 3.7%, respectively. Together with the hydrogen content of the gas gap, this makes the RICH sensitive to neutral particles. The fluxes of gammas and neutrons are, respectively, one and two orders of magnitude higher than that of charged particles.

In order to evaluate and optimize the RICH performance it is mandatory to estimate the contribution of the charged and neutral particle background to the overall occupancy. This task has been performed using the GEANT 3.21 based implementation of the RICH response simulation [2], and the FLUKA based ALICE simulation of the radiation environment [3, 4]. The two programs are combined to calculate the expected occupancy of the RICH.

## 4.2.2 GEANT description of the RICH

To simulate the performance in the ALICE radiation environment, a description of the RICH has been implemented into the ALICE GEANT 3.21 based detector simulation code, GALICE [5]. The program uses the GEANT routines GGCKOV and GTCKOV for the generation and tracking of Cherenkov photons.

The modelling of the RICH response, including the important photon feedback contribution, is based on the stand-alone code *richsim* that has been described in Chapter 2 and in Ref. [6]. In addition to the original code we explicitly track feedback photons and take into account the response of charged tracks with a large angle of incidence ( $\tan \theta_{\text{inc}} > \text{padsizesize/gapsizesize}$ ). Through the simulation of hadronic and electromagnetic interactions in the RICH, the GEANT implementation allows us to evaluate the detector response to gammas and neutrons.

### 4.2.2.1 Geometry

The RICH geometry defined for GEANT comprises the layered structure of the active part and the frames of the modules. The active part includes dead regions due to spacers and boundaries between radiator modules. The wire grid is not part of the geometry but its absorption effect is taken into account during tracking. The backplane of the RICH, i.e. photocathode, pad-plane and electronics, is implemented as one volume with tracking medium attributes including the Cherenkov photon detection efficiency and the average material thickness. The cathode segmentation is assumed to be  $162 \times 162$  pads per module and a pad size of  $8 \times 8 \text{ mm}^2$  is taken into account at the signal generation level.

#### 4.2.2.2 Background processes

The production of background events from gamma conversions or hadronic interactions in any of the detector planes is taken into account automatically by GEANT during tracking. By setting the kinetic energy threshold for the tracking to its lowest value (50 keV for gammas, electrons and positrons), we got the best possible description of the background in a high-radiation environment. The background due to feedback photons has been described as explained in Section 2.4.1.

#### 4.2.2.3 Signal generation

The signal generation described in Section 2.4, has been complemented by specific tracking of background tracks and photons.

Background particles may have any angle of incidence and the ionization along their path may induce charges over many pads. In such cases the signal generation is followed over the whole path within the MWPC gap.

An example of a simulated background event is shown in Fig. 4.2. In this event a 350 GeV/ $c$  charged pion has undergone a hadronic interaction in the RICH backplane. One of the produced secondary particles travels nearly parallel to the cathode plane and produces a long track.

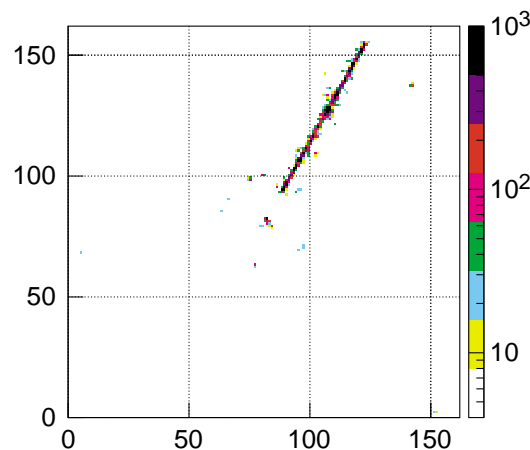


**Figure 4.2:** Simulated RICH response to a hadronic interaction in the backplane.

#### 4.2.2.4 Electronics noise and zero-suppression

In the output produced by GALICE, the induced charge per pad is stored separately for each hit. From this information the *digit* of each pad is obtained by summing up the individual contributions from all hits and then adding random noise and applying zero suppression. This procedure allows, in case of overlapping hits, to determine in an analysis program the individual contributions to the hits and evaluate their influence on occupancy, pattern recognition and angular resolution.

For the simulation results presented here we added random noise with a r.m.s. of 1 ADC channel (in the following we use the unit ADC chan, where 1 ADC chan = 0.17 fC). The pad-to-pad variation of the noise r.m.s. is 0.12 ADC channels. A threshold of 5 ADC channels is applied.

#### 4.2.2.5 Comparison with test beam data

A comparison of the simulation results of the RICH response to 350 GeV/ $c$  pions with results from test beam data, relevant for the evaluation of the occupancy (number of clusters, cluster size and integrated pulse height), is shown in Table 4.1. The overall agreement of the simulation with the test is very good.

**Table 4.1:** RICH response to single pions when comparing data and simulation for a single-electron mean pulse-height of  $A_0 = 43$  ADC chan.

	Data	Simulation
Photon fiducial region		
Resolved clusters	16	15.5
Cluster size	2.0	1.9
Total charge (ADC chan)	968	928
MIP region		
Cluster size	5.5	5.3
Cluster charge (ADC chan)	982	1096
Outside fiducial and MIP		
Clusters	1.5	1.45
Cluster size	1.5	1.8
Total charge (ADC chan)	100	83

### 4.2.3 Background simulation

Charged and neutral background particles for the HMPID are produced in structural elements (absorber, beam-pipe flanges) and other detectors, although they are not in the direct path of the primary particles reaching the detector. GEANT and FLUKA simulations have been performed to calculate the expected flux of background particles. Both simulations use a coarse description of the ALICE geometry outside the RICH, representing the material budget to our best knowledge. The GEANT simulation includes a detailed description of the RICH and its response, as described in the previous section. The present version of FLUKA does not provide any generation or tracking of Cherenkov photons. Hence, the simulation of the detector response is not possible within the same program. The momentum vectors from FLUKA are used as an input to GALICE, where the detector response is simulated in a second step.

FLUKA [3] was run with the EMF option for explicit electromagnetic shower evolution. Close to the material surfaces, the gamma and electron kinetic energy cuts were set to 50 and 100 keV, respectively. Higher cuts were used in shielded regions in order to decrease the calculation time. Neutrons were produced and tracked down to thermal energies. All other particles were tracked down to a kinetic energy of 1 MeV.

The same kinetic energy cuts were used in the GALICE simulations except for neutrons which are only tracked down to a minimum kinetic energy of 10 keV. The GEANT/MICAP interface [7] has been used to simulate the RICH response to low-energetic neutrons resulting from the FLUKA simulation.

The primary particle flux has been simulated by sampling from pion and kaon pseudorapidity distributions obtained from the HIJING event generator, as described in Ref. [8]. The normalization was adjusted to obtain 8000 charged particles per unit of rapidity in the central region.

## 4.2.4 Results

### 4.2.4.1 Charged and neutral particle fluxes

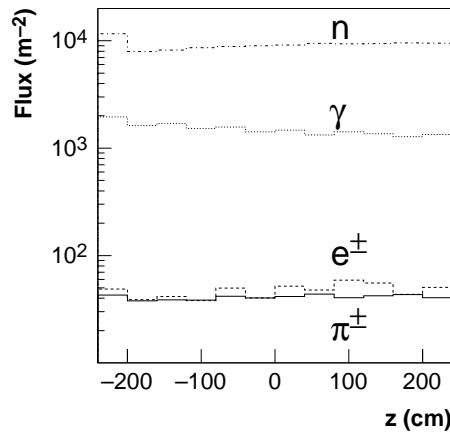
A breakdown of the charged and neutral particle fluxes at the radial position of the RICH, as obtained with FLUKA, is shown in Table 4.2. The flux of primary pions and kaons amounts to  $32.2 \text{ m}^{-2}$  and  $1.4 \text{ m}^{-2}$ , respectively. A similar contribution to the charged particle flux comes from electrons and positrons ( $43 \text{ m}^{-2}$ ). The proton flux is low ( $3.7 \text{ m}^{-2}$ ), but a potential increase in occupancy may result from their stronger ionization loss. Only 8% of the charged particles enter the RICH from above, i.e. backscattering from the L3 magnet.

**Table 4.2:** Neutral and charged particle fluxes from a central Pb–Pb collision at  $R = 4.8$  m

Particle	Flux ( $\text{m}^{-2}$ )	Flux from below ( $\text{m}^{-2}$ )
All $\pi^\pm$	40.7	39.6
Primary $\pi^\pm$	32.2	32.2
Primary $\pi^\pm$ ( $p > 1 \text{ GeV}/c$ )	4.6	4.6
All $K^\pm$	1.40	1.40
Primary $K^\pm$	1.33	1.33
Primary $K^\pm$ ( $p > 1 \text{ GeV}/c$ )	0.59	0.59
$\mu^\pm$	14.1	12.3
Electrons	28.7	25.8
Positrons	15.0	12.6
Protons (secondary)	3.69	3.27
All charged	103.5	95.0
All $\gamma$	1490	1030
primary $\gamma$	120	120
$\gamma$ ( $E_\gamma > 1 \text{ MeV}$ )	560	390
All neutrons	9100	4970
Neutrons ( $E_{\text{kin}} > 100 \text{ keV}$ )	3100	2060
Thermal neutrons	205	130

The  $\gamma$  flux amounts to  $1500 \text{ m}^{-2}$ . Most of the  $\gamma$ 's are products from secondary interactions. About 30% of the total flux is shining from the L3 magnet back onto the RICH.

The total neutron flux amounts to  $9100 \text{ m}^{-2}$ , out of which 34% are neutrons with kinetic energies above 100 keV and 2% are thermal neutrons. The fast neutrons can create a signal by knocking out a proton from the methane gap. Nearly the same amount of neutrons reach the RICH from below as from above.

**Figure 4.3:** Charged and neutral particle fluxes as a function of the  $z$  coordinate along the beam axis, as simulated with FLUKA. The absorber of the muon spectrometer is on the positive side.

The fluxes of charged particles, gammas and neutrons as a function of the position along the beam axis ( $z$ ) are shown in Fig. 4.3. Some asymmetries with respect to the interaction point ( $z = 0$ ) can be observed due to the presence of the front absorber (from the muon spectrometer) and of the ITS services.

#### 4.2.4.2 Event displays

The map of hit pads of one module for a central Pb–Pb collision is illustrated in Fig. 4.4. The single-electron mean pulse-height for this event is 20 ADC chan. and the proximity gap distance corresponds to a saturation ring radii of 155 mm. Under these conditions 9.3% of the pads have a signal above the threshold. To get an impression of the influence of the background hits, we show in Fig. 4.5 the hit pattern produced by primary charged pions alone. In this case the occupancy amounts to only 4%. Figure 4.6 shows the ring pattern created by pions with momenta above 1 GeV/c.

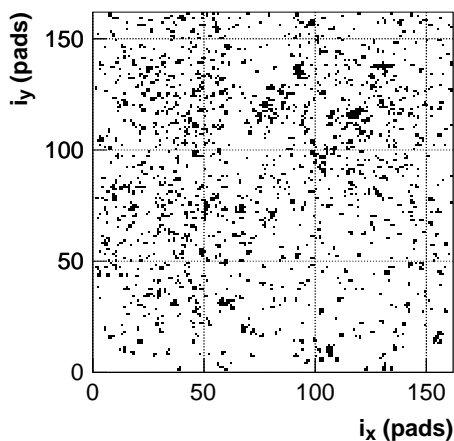


**Figure 4.4:** Simulated full event (Pb–Pb central collision) as seen by a RICH module.

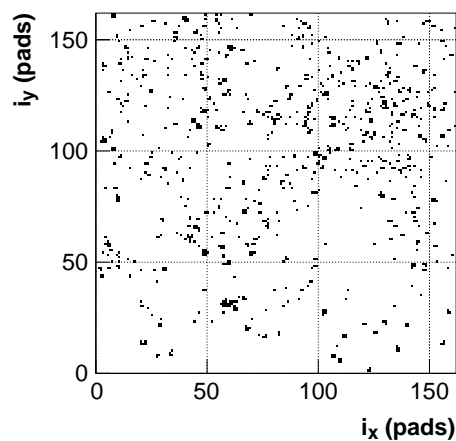


**Figure 4.5:** Same as Fig. 4.4, but for primary charged pions only.

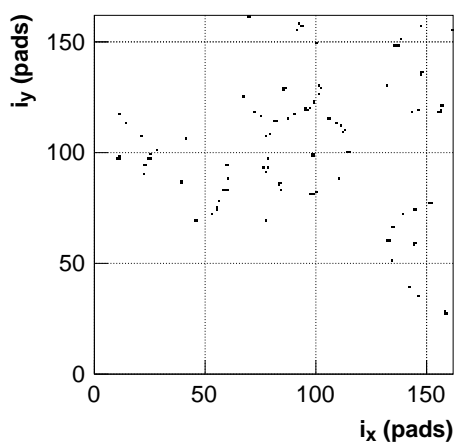


**Figure 4.6:** Same as Fig. 4.4, but for primary charged pions with  $p > 1$  GeV/c only.

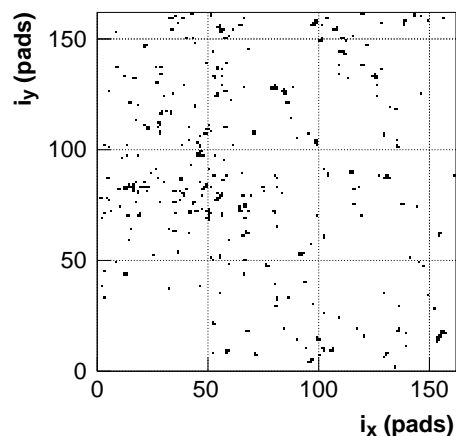


**Figure 4.7:** Same as Fig. 4.4, but for gammas only.

The pattern produced by gamma conversions in the RICH alone is shown in Fig. 4.7. As for hadronic interactions, backscattering from the cathode plane can produce track segments as can be seen in the lower right part of the picture. Conversions in the quartz window can produce pairs of MIP clusters, which are likely to overlap. Conversion in the radiator or in front of it can produce double rings (see Fig. 4.8).

As will be shown in the next section, the contribution of neutrons to the overall occupancy is small. Locally, however, the knock-out of a proton by a fast neutron can lead to a substantial release of charge creating a large pad cluster, as can be seen from Fig. 4.9.

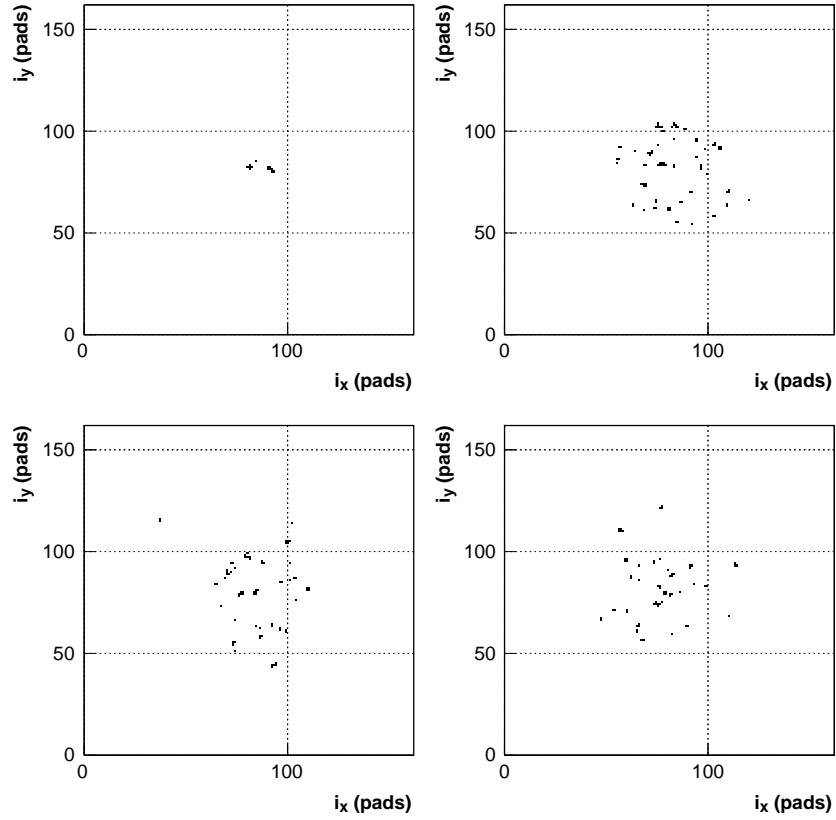


**Figure 4.8:** Examples of single gamma interaction in the RICH radiator ( $E_\gamma = 100$  MeV).

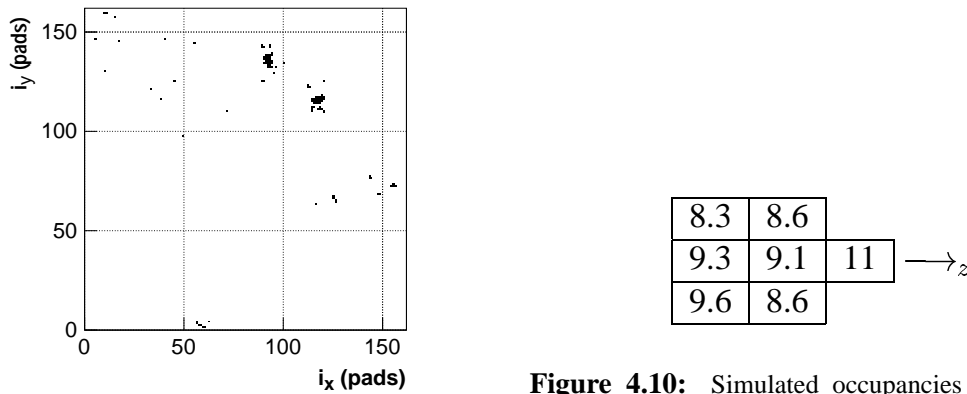


**Figure 4.9:** Same as Fig. 4.4, but for neutrons only.

**Figure 4.10:** Simulated occupancies (%) of the seven RICH modules for one central Pb–Pb collision (single electron mean pulse height: 20 ADC chan).

#### 4.2.4.3 Occupancy

The occupancies for each of the seven RICH modules as obtained from one simulated central Pb–Pb event (single-electron, mean-pulse-height 20 ADC chan) are shown in Fig. 4.10. The average occupancy amounts to 9.23% at a mean single-electron pulse height of  $A_0 = 20$  ADC chan.

The effect on the occupancy caused by the change of the single-electron mean pulse height from 10 ADC chan to 40 ADC chan is demonstrated in Table 4.3. Decreasing the amplification will also decrease the number of signal hits. Hence, the choice of the amplification has to come from an optimization of pattern recognition efficiency and resolution.

Finally, we show in Table 4.4 the relative contributions of the different particle species to the occupancy. The values were obtained by observing the decrease in occupancy when the respective particle was taken out of the total flux. Half of the occupancy results from pions and decay muons. Primary pions and kaons alone give an occupancy of 3.2%.

**Table 4.3:** Simulated mean occupancy as a function of the single-electron mean pulse height  $A_0$

$A_0$ ( ADC chan.)	Mean Occupancy (%)
10	5.6
20	9.2
30	11.2
43	12.7

**Table 4.4:** Simulated contributions of individual particle fluxes to the mean occupancy

Particle	Contribution in %
pions	37
$\mu^+, \mu^-$	13
photons	22
$e^+, e^-$	23
neutrons	4

### 4.3 Pattern recognition

In the following we present the status of the pattern recognition algorithm that has been developed specifically for the HMPID. A geometrical reconstruction of the photon angles has been developed using sets of samples of controlled density, in order to transform the coordinate space of clusters in the pad plane to a Cherenkov angle parameter space. This method, based on the approach initially reported in Ref. [9], is very general and is valid for any track incidence on the RICH surface. The signal obtained in this manner has been treated in the frame of a ‘Hough-like’ pattern recognition method to determine for each track the corresponding mean Cherenkov angle. The development of the pattern recognition is important at the present stage because it serves to validate the design and allows further optimizations of the construction.

#### 4.3.1 Data sample used for pattern recognition

Different sets of data have been used in the current analysis. The main ones have been obtained as a superposition of single-track (beam) events, so that one obtains samples of known densities. The events are obtained by randomly superimposing a fixed number of single ring events on a pad map of the dimensions of the ALICE prototype module. In such a way, sets of respectively 10, 20, 30, 40 and 50 overlapped events per square metre have been formed, the last density being representative of the maximum expected pad occupancy in the ALICE environment. Only results obtained with the superposition of tracks perpendicular to the radiator will be presented in here, but sets of data under angles of incidence varying from 2.5 to 7.5 degrees are also available and will be analysed in the near future. Since special care was given to the study of the importance of the photon feedback on the pattern recognition, events measured at different anode voltages have been used. In addition, the influence of the ‘ring’ radius has been studied using different gaps. The different samples are summarized in Table 4.5. Another set of data has been

**Table 4.5:** Samples of data, collected at the SPS with a 350 GeV/c pion beam, used for the analysis

Sample	‘ring’ radius (mm)	Density ( $\text{m}^{-2}$ )	RICH-HV (V)
1	155	1, 10, 20, 30, 40, 50	2100
2	155	1, 10, 20, 30, 40, 50	2050
3	155	1, 10, 20, 30, 40, 50	2000
4	122	1, 10, 20, 30, 40, 50	2100

obtained from GALICE, as explained in the preceding section, for pattern recognition studies of simulated, multiple-track ALICE events.

Figure 4.11 shows overlapped events corresponding to sample (1), for different particle densities.

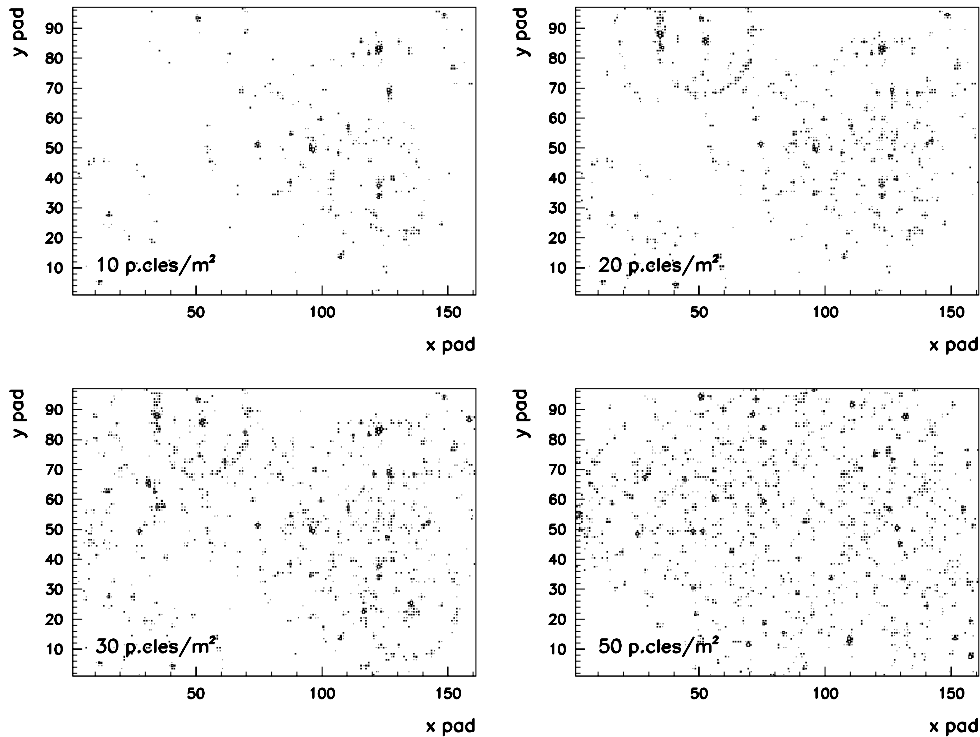


**Figure 4.11:** Overlapped events at different particle densities.

The occupancy for different radii and anode high voltages as a function of the number of overlapped events is shown in Fig. 4.12. The pad occupancy on the cathode plane depends on the ring radius, the HV setting on the MWPC and is proportional to the particle density. A particle density of 50 particles/m<sup>2</sup> corresponds to an occupancy of  $\sim 12\%$ , equivalent to the largest occupancy obtained in Section 4.2.4.3 from the GALICE simulation, where most of the particles have low momenta and large angles, therefore emitting a smaller number of photons in the detector than in the case of the test beam tracks.

The fact that the occupancy is higher at smaller radii is understandable in terms of ‘edge effects’. The larger radii get a smaller number of full rings into the detector active area than is the case for smaller radii.

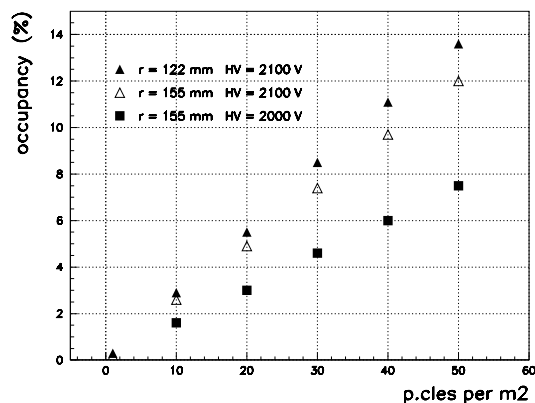


**Figure 4.12:** Occupancy on the photocathode for different conditions of gap size and anode voltage.

### 4.3.2 The signal from the HMPID readout: the pad hit and the clusters

The signal recorded by the pad readout of the MWPC consists of the following information:

- the coordinates of the pads where a signal (after zero suppression) has been recorded. We call them *hit pads*;
- the amount of charge induced on each hit pad, obtained by the analog readout of the electronics.

Because of the nature of the induction process (the characteristic spread), the pad size ( $8 \times 8 \text{ mm}^2$ ), and the fluctuation of the charge in the avalanche, the signal produced by a single-track ionization in the gas or by Cherenkov photons converted in the CsI layer on the cathode will result in a ‘cluster’ the size of which may vary from one to several pads.

### 4.3.3 Cluster centroids and deconvolution

The map of hit pads is first analysed for clusters by an algorithm that recognizes, as such, groups of adjacent hit pads that share one common edge. In a second pass, the identified clusters are analysed looking for the existence of possible multiple-charge maxima in a single cluster, indicating that the recognized cluster represents, in fact, an overlap of two or more clusters. In cases where multiple maxima are observed, a deconvolution algorithm is applied, resulting in so-called ‘resolved clusters’. Finally, a charge-weighted centroid is defined for each identified resolved cluster. Although this procedure allows a better localization of the photons, it does not mean that clustering can be usefully applied in high-occupancy environments; this point will be addressed in Section 4.3.6.

### 4.3.4 Reconstruction of the ‘Cherenkov signal’

In the most general case of multiple tracks on the HMPID we have:

- a large-sized map of hits with a very complex pattern where individual RICH patterns can hardly be identified by eye (see Fig. 4.11);
- a map of ‘impacts’ of tracks as extrapolated from the TPC to the HMPID cathode plane;
- a number of real impacts corresponding to large charge clusters close to the extrapolated impact points [10].

In order to extract the Cherenkov signal, for a chosen track, from the described cluster distribution and track-impact information, we proceed as follows:

- we define a ‘*fiducial zone*’ on the detector plane where Cherenkov photon clusters emitted by the chosen track of known momentum and incidence angle may be observed;
- we associate to each cluster (or pad) in the fiducial area a ‘Cherenkov angle’ of emission in the radiator as if it were produced by the track.

The latter task is performed using a backtracing algorithm described in the next section.

#### 4.3.4.1 Geometrical backtracing

The backtracing reflects the fact that from a cluster centroid we try to reconstruct the angle under which the photon causing it could have been emitted if it had belonged to the chosen track. To be able to start backtracing we have to make the following assumptions:

1. the origin of ‘photons’ resulting in the same reconstructed angle is chosen to be one point on the track path through the radiator. The coordinates of this point vary with the angle (because of the absorption in the radiator) and are close to the middle of the radiator;

2. all the ‘photons’ are assumed to be of the same energy, corresponding to the mean energy of the photons producing photoelectrons in the HMPID RICH: 6.85 eV;
3. no assumption is made on the  $\beta$  of the particle.

The reference system has the origin at the entrance point of the Minimum Ionizing Particle (MIP) in the detector. As illustrated in Fig. 4.13, we define:

- $(x_p, y_p)$  = MIP impact coordinates projected onto the photocathode
- $(\theta_p, \phi_p)$  = MIP polar and azimuthal angles
- $(x, y)$  = photon impact coordinates projected onto the photocathode
- $(\theta, \phi)$  = photon polar and azimuthal angles
- $r_w, q_w, t_{gap}$  = radiator, quartz and gap widths
- $n_f, n_q, n_g$  = freon, quartz and methane refractive indices.

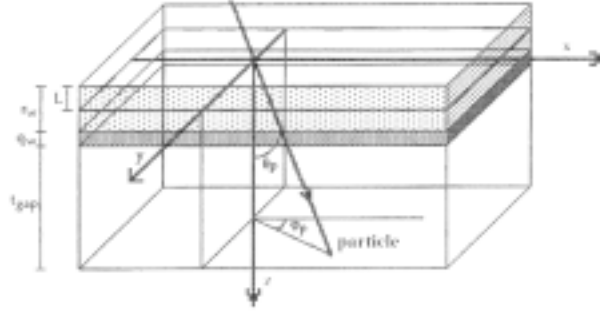


**Figure 4.13:** Reference system used in the backtracking.

The azimuthal angle  $\phi$  for the photon can be evaluated, assuming an average emission depth  $L$  (at the middle of the radiator):

$$\tan \phi = \frac{y - L \tan \theta_p \sin \phi_p}{x - L \tan \theta_p \cos \phi_p} . \quad (4.1)$$

Using this value of  $\phi$  and defining  $a$  and  $R$  as

$$\begin{aligned} a &= [(r_w - L) + q_w + t_{gap}] \tan \theta_p \\ R &= \text{distance MIP — photon cluster on the photocathode} , \end{aligned}$$

the following equation has to be solved:

$$R^2 = [a \cos \phi_p - b \cos \phi]^2 + [a \sin \phi_p - b \sin \phi]^2 . \quad (4.2)$$

In Eq. (4.2)  $b$  is a function of the polar angle of the photon according to

$$b = (r_w - L) \tan \theta + q_w \frac{n_f \sin \theta}{\sqrt{n_q^2 - n_f^2 \sin^2 \theta}} + t_{gap} \frac{n_f \sin \theta}{\sqrt{n_g^2 - n_f^2 \sin^2 \theta}} . \quad (4.3)$$

Therefore, the solution of Eq. (4.2) taking into account Eq. (4.3) provides the value of  $\theta$  for the current photon of the MIP.

Finally, the Cherenkov angle  $\eta_c$  for the photon is calculated by:

$$\cos \eta_c = \sin \theta_p \cos(\phi - \phi_p) + \cos \theta_p \cos \theta . \quad (4.4)$$

### 4.3.5 Analysis of single beam events

Single-beam events at the SPS have been processed in order to obtain the Cherenkov angle resolution in the absence of background coming from other tracks. In Fig. 4.14a the distribution of extracted Cherenkov angles per cluster, using the described method, is shown for data sample (1) (see Table 4.5): there is a clear signal with negligible background). The Gaussian fit of the distribution gives a  $\sigma_{\eta_c} \sim 12.8$  mrad.

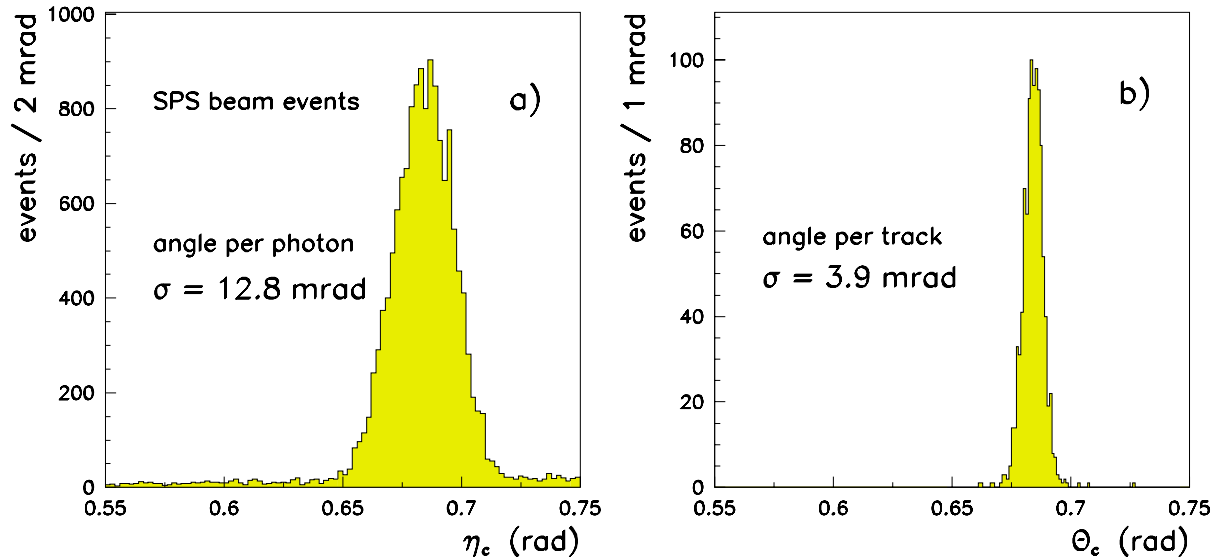


**Figure 4.14:** Photon angle distribution (a) and track Cherenkov angle distribution (b) for beam events at the SPS in data sample (1).

By averaging the  $\eta_c$  for all the photons, the mean Cherenkov angle per track  $\theta_c$  is obtained: the distribution, shown in Fig. 4.14b, indicates this resolution to be 3.9 mrad. The distribution in Fig. 4.14b has been obtained considering only photons with  $\eta_c$  angle ranging between 0.550 and 0.750 rad. This fiducial area has no special meaning — it is meant to shorten the computing time.

To determine the baseline parameters we show in Fig. 4.15 the resolved cluster multiplicity, cluster size, and charge spectrum for the case of single-event patterns.

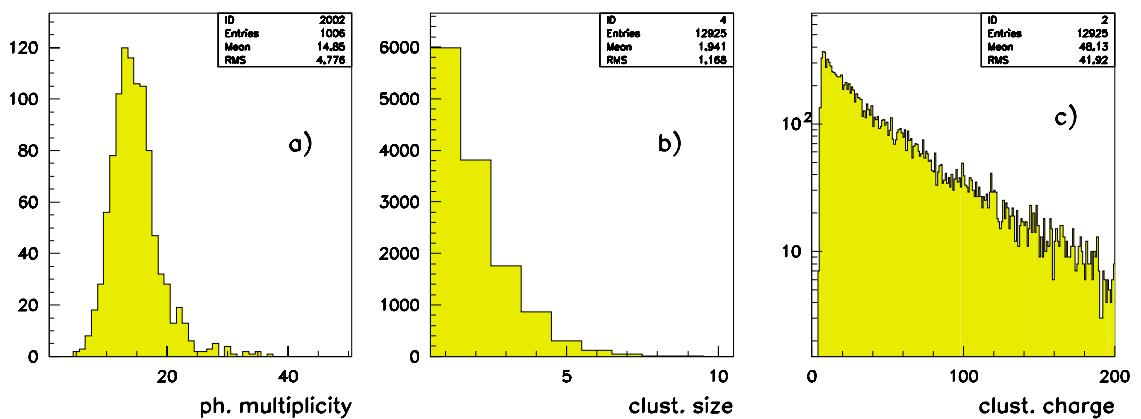


**Figure 4.15:** Photon cluster multiplicity (a), cluster size (b), and charge (c).

### 4.3.6 Analysis of overlapped data sets

#### Pad or cluster centroid backtracing

Although at first sight it seems advantageous to use the cluster centroid method in the backtracing algorithm (better localization) it has been observed that this method, even at moderate densities, leads to a reduction of the Cherenkov signal. The reasons for that are obvious — partially overlapping clusters from different tracks will merge into single clusters thereby reducing the overall number of clusters, and hence leading to a wrong centroid determination. For these reasons, we have analysed multi-ring events taking into the backtracing algorithm only the hit pads, assuming as photon-pad location the middle of the pad itself.

#### Fiducial region

Starting from the MIP position and knowing the detector parameters, a wide fiducial region is defined, around the MIP impact where all the photons relevant to that track could eventually be found. In the present analysis we have chosen to backtrace all pad hits corresponding to photon angles between 0.550 and 0.750 rad.

As an example, we can see in Fig. 4.16a the map of all backtraced photons (the MIP impact position is always in the origin), i.e. the assumed fiducial band: the picture corresponds to a density of 10 particles/m<sup>2</sup> from sample (1).

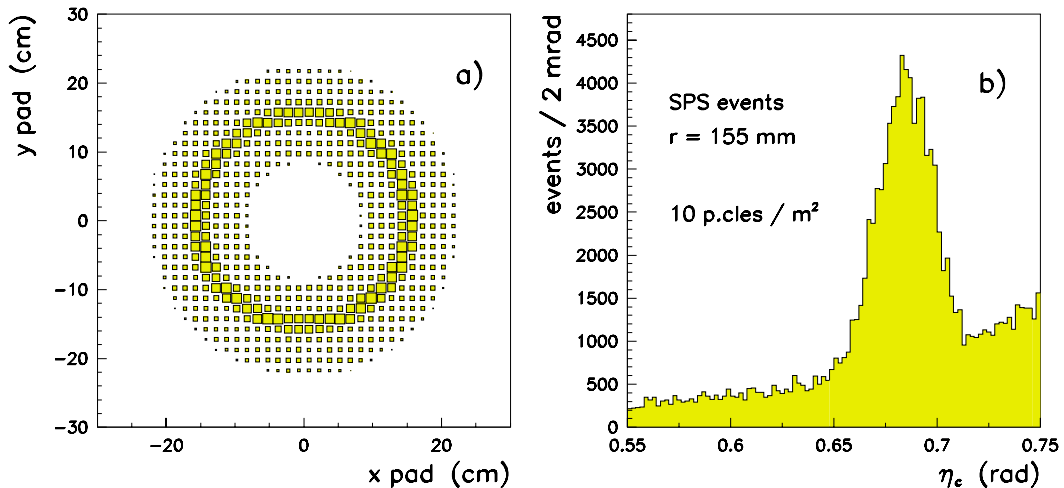


**Figure 4.16:** Fiducial band around the MIP (a) and photon angle distribution (b) at 10 particles/m<sup>2</sup> for sample (1).

The  $\eta_c$  distribution in Fig. 4.16b shows two distinct components: the peak around the Cherenkov angle, produced by photons belonging to the tracks analysed, and a continuous background belonging to photon pads produced by other tracks and falling in the analysed fiducial zone. The increasing profile of the background distribution is expected and is mainly due to the fact that at larger  $\eta_c$  values, a larger surface of the plane is covered for equal  $\eta_c$  bins. The shape of the background distribution is a challenge to the pattern recognition — biasing the peak value of the distribution towards higher angles. We therefore have to carefully treat the background in the analysis.

#### 4.3.6.1 Background treatment

The background has been parameterised with an analytical form:

$$F_{bkg}(\eta_c) = [\tan \eta_c (1 + \tan^2 \eta_c)]^\alpha + A + B \tan \eta_c, \quad (4.5)$$

where  $\alpha = 5.52$ ,  $A = -7.80$  and  $B = 22.02$ . This parametrisation fits equally well all the studied densities.

With this analytical form, each photon has been weighted according to the following procedure. For each analysed track (MIP impact) the corresponding  $\eta_c$  distribution is calculated. In this distribution we calculate the number of photons  $N_{bkg}$  in a sampling band far from the signal (i.e. with  $\eta_c$  between  $\eta_{bkg}^1 = 0.720$  and  $\eta_{bkg}^2 = 0.760$  rad).

So the expected amount of background photons at any  $\eta_c$  can be estimated by means of Eq. (4.5), as

$$R_{bkg}(\eta_c)d\eta_c = \frac{F_{bkg}(\eta_c)N_{bkg}}{\int_{\eta_{bkg}^1}^{\eta_{bkg}^2} F_{bkg}(\eta'_c)d\eta'_c}d\eta_c, \quad (4.6)$$

In Eq. (4.6)  $d\eta_c$  is 1 mrad and  $R_{bkg}(\eta_c)d\eta_c$  is the expected amount of background photons in a 1 mrad bin at the angle  $\eta_c$ . In Fig. 4.17 we show the fitted background (dashed line) compared with the real background shape at several particle densities. The white distribution in each case corresponds to the photon  $\eta_c$  spectrum obtained for all analysed MIPs.

If  $N_{ph}(\eta_c)d\eta_c$  is the  $\eta_c$  spectrum for the MIP under study, then in order to take into account the background, each photon in each bin should be weighted by

$$W_{bkg}(\eta_c) = 1 - \frac{R_{bkg}(\eta_c)}{N_{ph}(\eta_c)}. \quad (4.7)$$

The dark distributions in Fig. 4.17 have been obtained by entering each photon with the corresponding weight calculated by Eq. (4.7). In this way the background contribution has been taken into account so that, a priori, no systematic biasing of the signal will occur in the pattern recognition.

#### 4.3.6.2 Extraction of the mean Cherenkov angle

The determination of the mean Cherenkov angle per track is the main goal of the pattern recognition. The  $\eta_c$  signal observed in Fig. 4.17 shows that there is no drastic deterioration of the width of the signal distribution, but the mean Cherenkov angle is influenced by the presence of the background signal. In the following we will shortly review the steps in the pattern recognition that we have developed. Our basic approach is to apply a Hough transform method which has been modified to accommodate the fact that the signal in the  $\eta_c$  coordinate has a natural width given by all the features described in Chapter 2. To account for that width we apply a *sampling band* approach that consists in sliding a window of a width comparable to the width of the signal over the  $\eta_c$  spectrum. At each step in the sliding, the number of pads found within the window is counted. When the window reaches the region for which the number of counted photon-pads is the largest, the content of the window is called the '*Hough selected photon pads*'. Using that information and the known background weights, an iterative averaging procedure is used to finally determine the value of the mean Cherenkov angle associated to that track.

#### The Hough Transform method

The pattern recognition for the HMPID, on the track level, has been implemented using the Hough technique to extract the mean Cherenkov angle per track as a parameter to be estimated in a transformed parametric space [11, 12].

The Hough Transform method (HT) is an efficient implementation of a generalized *template matching* strategy for detecting complex patterns in binary images. This is achieved by analysing the parameters which characterize these patterns and looking for local maxima in a *feature parameter space* [13]. The main advantage of the Hough transform is that it is relatively unaffected by topological gaps in curves

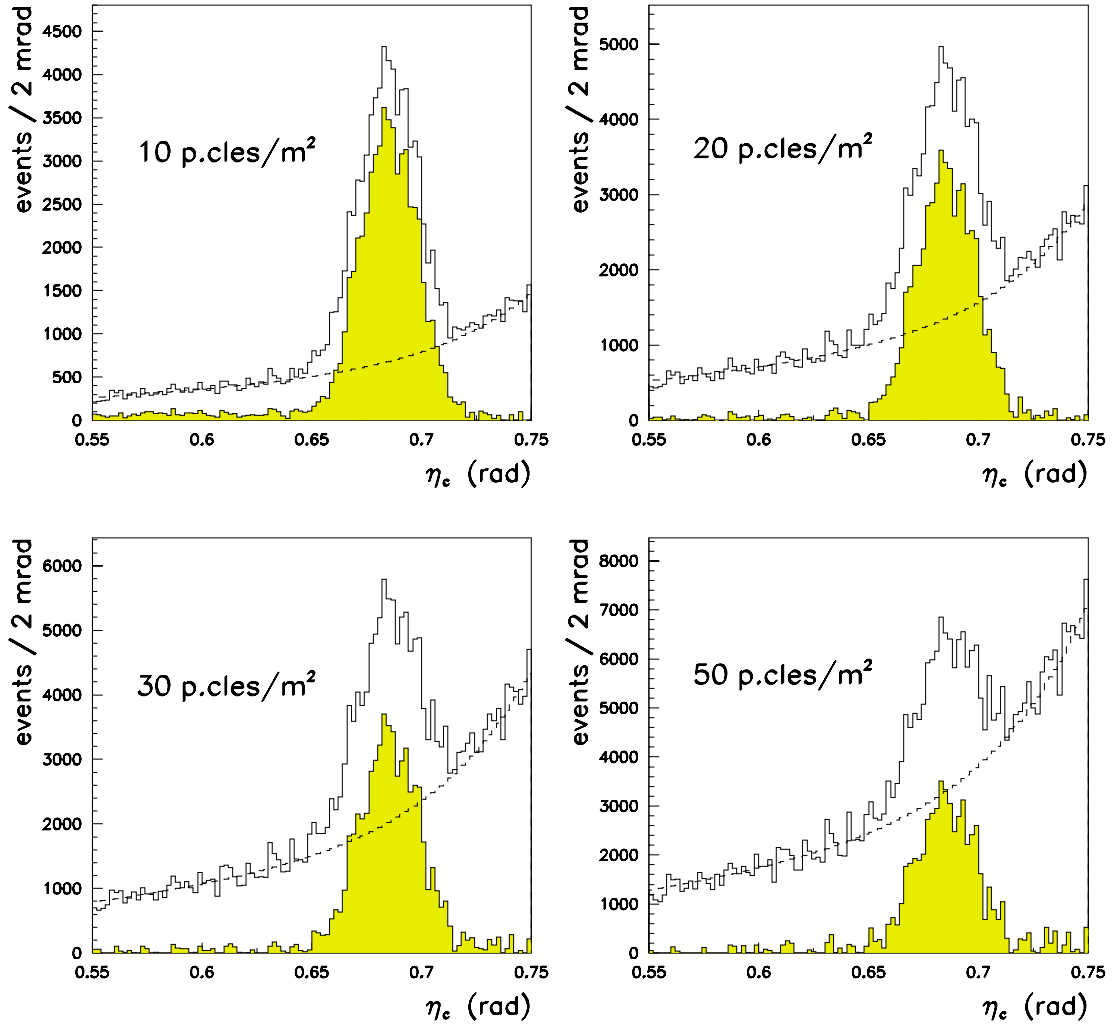


**Figure 4.17:** Distributions of  $\eta_c$  per photon-pad at different particle densities, with estimated (dashed) and subtracted (dark) background for sample (1).

and by high-noise background in spot-like images [14]. In general, let us assume that we transform a Cartesian space into a feature space:

$$\mathbf{x} \rightarrow (\mathbf{a}, T(\mathbf{x}, \mathbf{a})) , \quad (4.8)$$

where  $\mathbf{a}$  is a parameter vector and  $T(\mathbf{x}, \mathbf{a})$  its relative transform. For each thresholded contribution of  $T(\mathbf{x}, \mathbf{a})$  in the parameter space, a Hough counting takes place in the so-called ‘*Hough Counting Space*’ (HCS):

$$HCS(T(\mathbf{x}, \mathbf{a})) := HCS(T(\mathbf{x}, \mathbf{a})) + w , \quad (4.9)$$

where  $w$  is a given weight to be assigned to the *feature vector*  $\mathbf{a}$  which, in the simplest case, is assumed to be unitary. The *incrementation strategy* of Eq. (4.9) can be also further refined by applying an *incrementation function*:

$$w = w(\mathbf{x}, \mathbf{a}) , \quad (4.10)$$

which implements a weighting policy in such a way as to use other relevant information associated with a given feature point [15]. The Hough estimator for the feature vector is given by the bin value in HCS which provides the highest occurrence in the parameter space.

For the HMPID analysis we have

$$(x, y) \rightarrow ((x_p, y_p, \theta_p, \phi_p), \eta_c) . \quad (4.11)$$

If we assume  $\mathbf{a} = (x_p, y_p, \theta_p, \phi_p)$  to be already known, the transform will reduce the problem to a solution in a one-dimensional mapping space. The HCS in this case represents the photon Cherenkov angle  $\eta_c$  spectrum and, indeed, a Hough estimator for the Cherenkov angle  $\theta_c$  of the particle is chosen as the highest peak provided by all the photons which fall in that angle bin. Thus, the HCS accumulates the contributions from several Cherenkov photons according to expression (Eq. 4.9). The analysis procedure can be easily extended and made more effective if the weight function (Eq. 4.10) is used to take into account other factors like the background evaluation or the charge contribution for each Cherenkov photon.

The transformation which provides the parameter  $\eta_c$  for a given vector  $\mathbf{a}$  has already been described in Section 4.3.4.1 as the *geometrical backtracing algorithm* to extract the Cherenkov angle associated to each photon pad. Each MIP cluster is excluded from this transformation and for each MIP cluster a scanning in the *MIP reference system* is done in such a way as to get the  $\eta_c$  values ranging from 0.550 to 0.750 rad. It should be noted that this kind of approach allows independence from the topological shape and size of the specific Cherenkov pattern cut in the plane of the detector (i.e. circular, elliptic, parabolic). This is due to the fact that the particle identification happens in the Cherenkov photon angle space, instead of the Cartesian one.

### HT method modified with correlation bands

The basic HT method applied to the HMPID has been enhanced in such a way as to be less influenced by the background caused from several noise sources [16].

For each photon there is a spread in the Cherenkov angle to be taken into account, which makes it harder to achieve a good resolution  $\sigma_{\eta_c}$  in the Cherenkov angle identification. In order to enhance statistically as much as possible the signal in the  $\eta_c$  spectrum, the incrementation expression (Eq. 4.9) has been modified.

The following integration in the  $\eta_c$  space over a *sampling band*  $b$  has been applied:

$$HCS'(\eta_c) = \int_{\eta_c - \frac{b}{2}}^{\eta_c + \frac{b}{2}} HCS(\eta'_c) d\eta'_c , \quad (4.12)$$

which, in the discrete case, where  $d\eta_c = 1$  mrad (i.e.  $\eta_c(k) = k$  d $\eta_c$ ,  $k$  integer), transform into the correlation:

$$HCS'(\eta_c(k)) = \sum_{i=\eta_c(k) - \frac{b}{2}}^{\eta_c(k) + \frac{b}{2}} HCS(i) . \quad (4.13)$$

The *HCS* has been calculated using  $w = W_{bkg}(\eta_c)$ , defined by (Eq. 4.7), as the incrementation function. The optimum sampling band in the correlation has been determined at 40 mrad for the smallest  $\sigma_{\eta_c}$  value.

The information extracted from the pattern recognition, for each analysed MIP, is the number of hit pads falling into the Hough selected band: we call those '*Hough selected photon pads*' and their number will be indicated by  $N_{ph}^{Hough}$ . In Fig. 4.18a these selected photon pads are shown in the case of a  $10 \text{ m}^{-2}$  particle density; in Fig. 4.18b the evolution of the  $N_{ph}^{Hough}$  distribution with the particle density is also reported.

In the pattern recognition the band selection performed by the Hough method, as described in Section 4.3.6, takes into account the background: this determines  $\theta_c^{Hough}$  and  $N_{ph}^{Hough}$ . Beyond that, we can also make use of the different  $\eta_c$  angles for the *Hough selected photon pads* and their background-related weights.

This information is used to calculate the average weighted angle as:

$$\langle \theta_c \rangle = \frac{1}{W_{tot}} \sum_{i=1}^{N_{ph}^{Hough}} W_{bkg}(\eta_c(i)) \eta_c(i) \quad W_{tot} = \sum_{i=1}^{N_{ph}^{Hough}} W_{bkg}(\eta_c(i)) . \quad (4.14)$$

In Fig. 4.19 the  $\theta_c$  distributions at three different densities are shown, with the bottom right plot re-summing (white triangles) the behaviour of the corresponding sigmas ('angle resolution' per MIP) versus particle density.

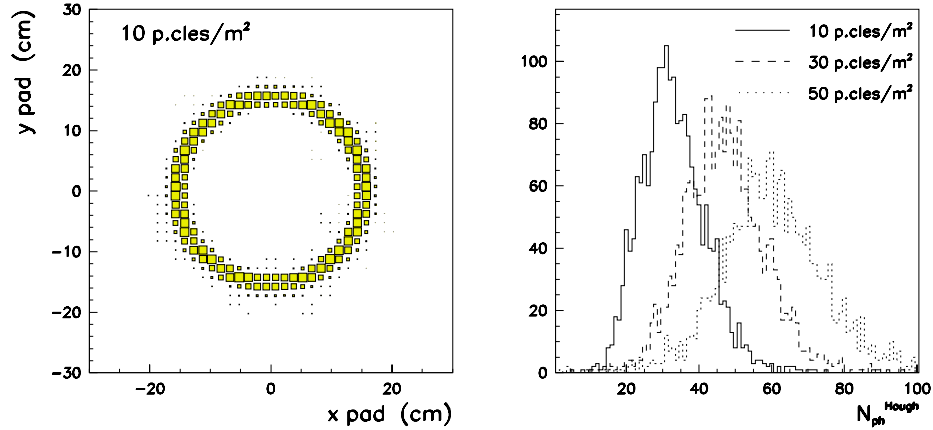


**Figure 4.18:** Hough selected photon pads at 10 particles/m<sup>2</sup> and multiplicity distributions at different densities for sample (1).

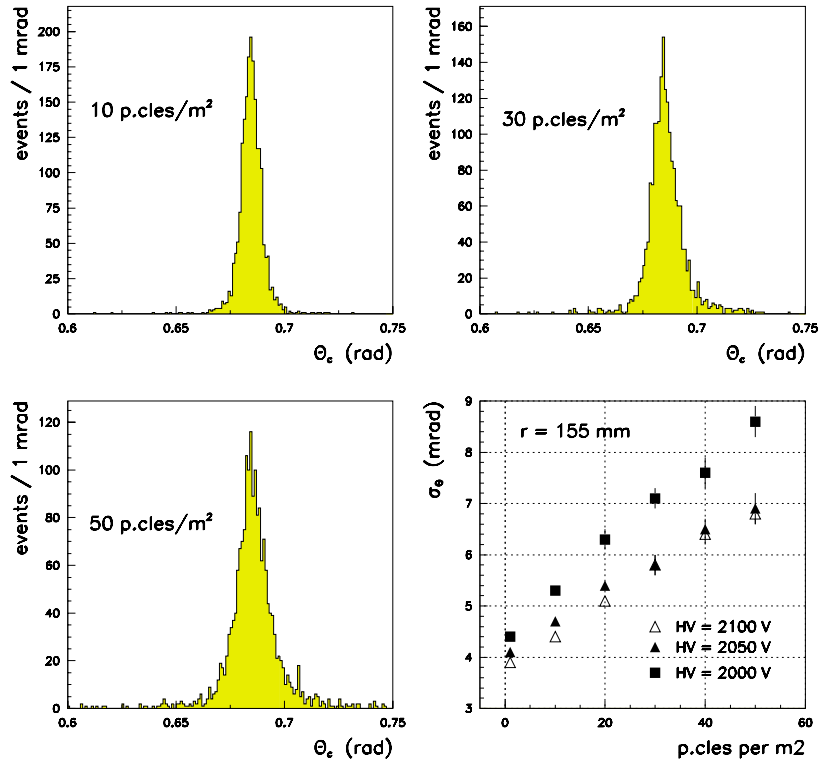


**Figure 4.19:** Final Cherenkov angle distributions per MIP at different densities for sample (1) and corresponding sigma evolution compared with those for samples (2) and (3).

The same analysis has also been applied for samples (2) and (3) in Table 4.5, i.e. overlapped beam

events collected at the SPS H4 beam in 1997 and 1998, lowering the RICH HV from 2100 V to 2050 V and 2000 V: the results are summarized in Fig. 4.19.

No significant difference is observed for the two higher HV values, while a degradation is observed at 2000 V, probably due to some photon losses at that voltage.

A ‘ring reconstruction efficiency’ can be extracted as the fraction of ‘good reconstructed rings’ with respect to the total number of MIPs: a well-reconstructed ring means that the corresponding Cherenkov angle falls within  $\pm 15$  mrad (i.e.  $\sim \pm 2\sigma$  of the angle distribution at the highest density) from the central value 0.686 rad. Figure 4.20 shows the evolution of this efficiency versus the particle density.

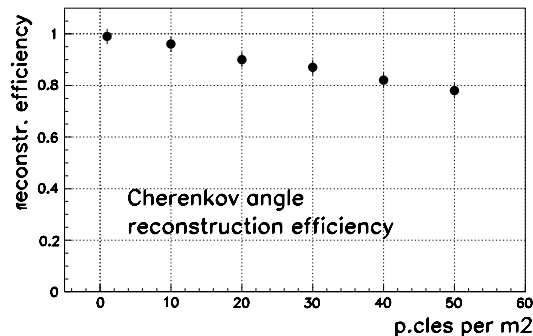


**Figure 4.20:** Ring reconstruction efficiency versus particle density for sample (1).

The same analysis has been applied to the event sample (4), the main aim being to study the dependence of the pattern recognition performance on the size of the single pattern (i.e. the ring radius). The behaviour of the  $\sigma_{\theta_c}$  versus the particle density is reported in Fig. 4.21a, where the results from sample (1) and sample (4) are compared.

The better resolution obtained for smaller  $R$  reflects the fact that the overlap of different patterns is smaller for smaller rings, hence the underlying noise background contribution is smaller. This result needs to be confirmed in the more general case of ‘realistic’ event simulations. In Fig. 1.4 the  $\theta_c$  distribution at 50 particles  $\text{m}^{-2}$  for sample (4) is shown, with the corresponding Gaussian fit of the peak.

The analytical relation between the Cherenkov angle resolution and the corresponding momentum limit for  $3\text{-}\sigma$   $\pi$ -K separation is plotted in Fig. 4.21b: it can be noted that in the best case the performance of the method provides a  $3\sigma$   $\pi$ -K separation up to more than 2.5 GeV/ $c$  for the most violent events anticipated in ALICE. Assuming the mean multiplicity of the recorded events to be about half the maximum value, the present analysis sets the  $3\sigma$   $\pi$ -K value to  $\sim 3$  GeV/ $c$ .

### 4.3.7 Recognition of Cherenkov patterns in the GALICE environment

The particle identification strategy of the HMPID will address only particles with a momentum larger than 1 GeV/ $c$ . With this in mind, the Hough transform method will never be applied to all particles in an event, as is the case in the analysis done so far, but it will concern limited regions in the HMPID plane where high-momentum particles are tracked by the TPC and the ITS.

As an example, we show the present pattern recognition applied to a well-defined hadron in the GALICE environment. The top part of Fig. 4.22 shows the map of hit pads belonging to one module of the HMPID, as simulated in GALICE for a Pb-Pb interaction.

In this high-density environment, Cherenkov patterns are not recognizable by eye. This is also true in the region enclosed by the box shown in the right-side part of the hit map. This box delimits a window opened around the hit point of a pion of 1.23 GeV/ $c$ , that impinges the HMPID plane at an incident angle of  $0.98^\circ$ .

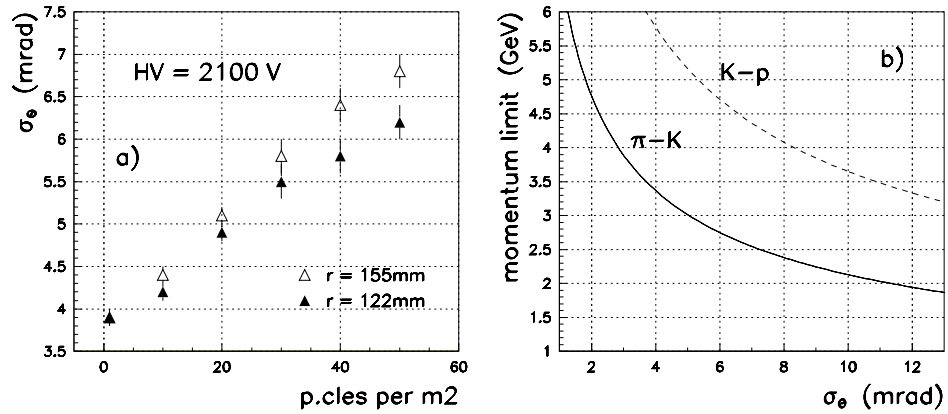


**Figure 4.21:** a) Cherenkov angle resolution vs. particle density at different radii; b) momentum limit vs.  $\sigma_\theta$ .

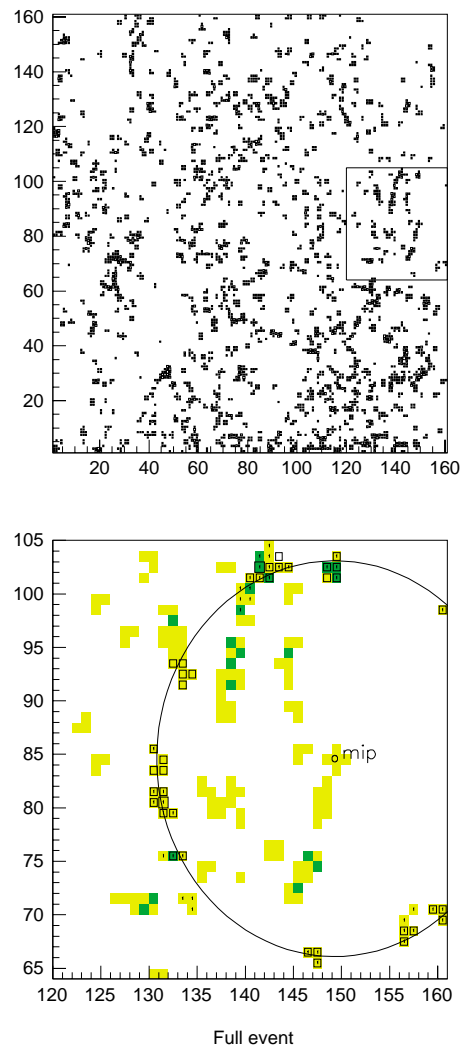


**Figure 4.22:** Top: hit map of one HMPID module in ALICE generated with the GALICE package for one Pb-Pb event. Bottom: zoom of the region enclosed by the box in the top map with the Cherenkov pattern (ring) associated to the Hough method.

In the lower part of Fig. 4.22, the particle hit point is indicated with ‘*mip*’ while the pads belonging to clusters initiated by the Cherenkov photons emitted by the selected particle are indicated as open boxes. The Hough Transform method has been applied to the set of clusters contained in the window.

Open boxes indicate pads of clusters initiated by Cherenkov photons associated in the pattern recognition to the particle that crosses the region in the point ‘*mip*’. Pads with a darker colour show overlap among clusters. Hough reconstructed pads are indicated with ‘1’. As shown, the method is able to recognize almost all the relevant clusters belonging to the Cherenkov photons. Indeed 30 pads out of 40 are associated to the right clusters, only one cluster has been completely missed due to the fact that it belongs to a huge unresolved cluster. The final result is a correct identification of the pion. A systematic analysis of GALICE events is in progress.

## 4.4 Matching of tracks with clusters on the HMPID pad plane

The pattern recognition of the Cherenkov patterns and the precision in the extraction of the Cherenkov angle rely heavily on the precise knowledge of the momentum of the particles, their angle of incidence, and impact point. In particular, it is of primary importance to demonstrate that, at the expected pad occupancy, we are able to correctly match the reconstructed tracks with the impact points at the HMPID pad plane, bearing in mind that the total charge allows to distinguish a MIP cluster from a photon cluster.

The tracking through the ITS and TPC and the extrapolation to the HMPID have been performed [10] by using simulated particles, with momenta ranging from 0.5 to 5 GeV/*c*. The points generated in the ITS and TPC detectors have been fitted in order to extract the kinematic parameters to be used for the extrapolation to the HMPID. After the calculation of the impact coordinates and direction cosines of the fitted track on the RICH module, the relevant quantities have been compared with those of the simulated track after its full evolution through the ALICE apparatus. These quantities have also been studied as a function of the track momentum.

### 4.4.1 Track simulation

Tracks have been generated with a flat momentum distribution, ranging from 0.5 to 5 GeV/*c* in the rapidity range  $|\eta| < 0.4$ . The evolution of the track through the ALICE subsystems (6 silicon layers in the ITS, 75 space points in the TPC region and the final set of RICH modules) has been determined by GEANT routines.

Multiple scattering in the beam pipe, silicon layers, TPC gas mixture and also in mechanical supports, cooling systems and in electronics has been taken into account (total equivalent to  $\sim 8\% X_0$ ) according to the detector design reported in the ALICE Technical Proposal [1] (see Table 4.6, where is shown the averaged material budget corresponding to the interesting momentum range for the HMPID as well as to ITS spatial acceptance). About 5000 tracks (over all momenta) have been processed, in an uniform magnetic field of 0.2 T within the RICH acceptance.

### 4.4.2 Track reconstruction

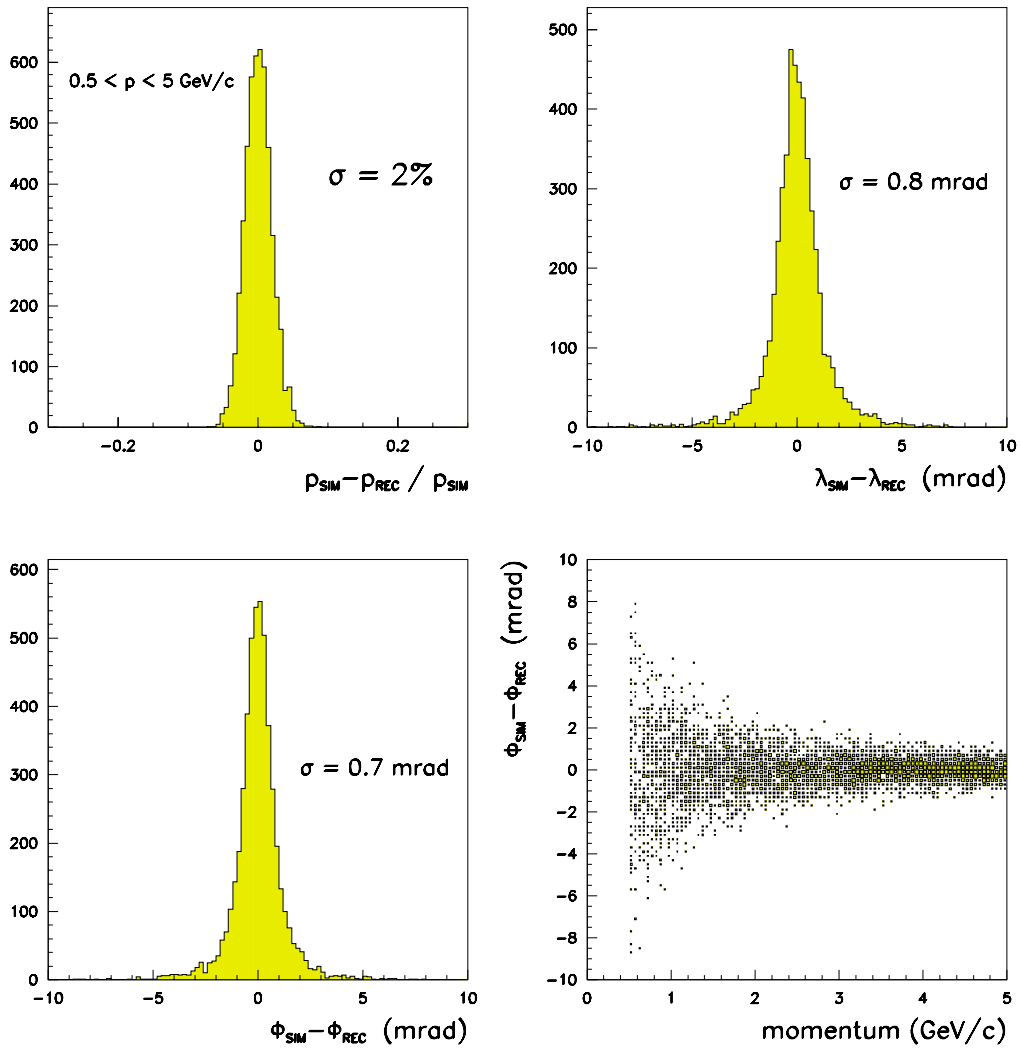
The fitting routines take into account the hits, both in the ITS and in the TPC detectors, according to the specification reported in the Technical Proposal [1].

In the fitting model the tracks are supposed to be helices [17] with a common vertex at (0,0,0), polar and azimuthal emission angles  $\lambda$  and  $\phi_0$ , respectively, and a radius of curvature  $R$  (cm) =  $p \cos \lambda / KB$  ( $K = 0.003$ ,  $B = 0.2$  T and track momentum  $p$  in GeV/*c*). All the hits (points in the fit) have been weighted, taking into account the detector spatial resolution and the multiple scattering error propagation through the different layers.

In Fig. 4.23 we report the distributions of the residuals between simulated and reconstructed track kinematic parameters. After reconstruction, angular resolutions of less than 1 mrad have been found,

**Table 4.6:** Averaged material budget in the tracking volume

	Radius (cm)	$X/X_0$ (%)		Radius (cm)	$X/X_0$ (%)
ITS			TPC		
Beam pipe	3.0	0.17	Inner vessel	52	0.27
Si pixel 1	3.9	0.64	CO <sub>2</sub>	52–78	0.14
Si pixel 2	7.3	0.64	Inner cage	78	0.52
Si drift 1	14	0.64	Working gas	78–250	0.56
Si drift 2	24	0.64	Outer cylinder	250	1.33
Si strip 1	40	0.64	Air	250–480	0.75
Si strip 2	45	0.64			
Outer shell	50	1.00			
Air	3–52	0.16			

**Figure 4.23:** Residuals of simulated and reconstructed kinematic parameters.

while the average  $\Delta p/p$  (over all momenta) is about 2%. These values are compatible with the tracking resolution estimates reported in the Technical Proposal. The  $\Delta p/p$  versus  $p$  behaviour will be discussed later in this Chapter.

The track fit residuals have been calculated for each detector layer; in particular, it is interesting to look at the residuals on the last pad row of the TPC, which is the end of the track measurement region. Figure 4.23 reports the distribution of the difference in  $r\phi$  and  $z$  coordinates between the fitted crossing point and the ‘data’ point; they refer to the whole sample, while Table 4.7 resumes the values of the sigmas of these distributions as a function of the track momentum.

**Table 4.7:** Sigmas of the residual distributions at the end of the TPC

Momentum range (GeV/c)	0.5–1	1–1.5	1.5–2	2–3	3–4	4–5
$r\phi$ -residuals ( $\mu\text{m}$ )	410	300	220	210	180	170
$z$ -residuals ( $\mu\text{m}$ )	1060	660	450	320	230	210

### 4.4.3 Extrapolation to the HMPID

#### 4.4.3.1 Evaluation of the tracking errors at the HMPID

A reconstructed track can be extrapolated from the last measured point in the TPC up to the HMPID modules by using the fitted kinematic parameters. Track-by-track impact coordinates and momentum vector components at the HMPID have been extracted: these have to be compared with real points and momenta provided by GEANT for the same detector module.

In the actual experiment the extrapolated impacts and directions are the starting point for the matching of track hits in the HMPID with the tracks in the TPC. It is useful to remember that the uncertainties in this determination are expected to be greatly amplified with respect to the fit residuals found at the end of the TPC: not only because of the fit error propagation along the 250 cm path from the TPC to the HMPID, but also because of the multiple scattering in the outer wall of the TPC vessel ( $\sim 1.3\% X_0$ ).

To estimate the final expected resolution on the impact and angles onto the RICH, we have to look at the distributions of the differences between extrapolated crossings and the ‘data’ point. Figure 4.24 shows the distribution of the difference  $\Delta(r\phi) = (r\phi)_{real} - (r\phi)_{extrap}$  and the same for  $\Delta z$  calculated at the RICH for all momenta (between 0.5 and 5 GeV/c).

The widths of these distributions provide the expected extrapolation error for  $r\phi$  and  $z$  coordinates of the track impact onto the RICH modules. The same calculation has been performed for the polar and azimuthal angles  $\lambda$  and  $\phi$  of the track. The following error estimates have been extracted:

$$\begin{aligned} \sigma_{r\phi} &= 3.3 \text{ mm} & \sigma_{\phi} &= 1.9 \text{ mrad} \\ \sigma_z &= 2.1 \text{ mm} & \sigma_{\lambda} &= 0.7 \text{ mrad} \end{aligned}$$

#### 4.4.4 Evaluation of the matching efficiency

We have investigated the probability of a fake match between the extrapolated track and the corresponding hit in the HMPID; this can occur due to the high hit density expected in the RICH modules in Pb–Pb events at the LHC.

A fake match occurs when another hit falls closer to the tracking prediction than the real impact of the track. The particle densities simulated as shown in Section 4.2 using the full ALICE detector material budget have reached a maximum density of 100 particles/m<sup>2</sup>. The amount of ‘mismatches’ computed as a function of track momentum is reported in Table 4.8.

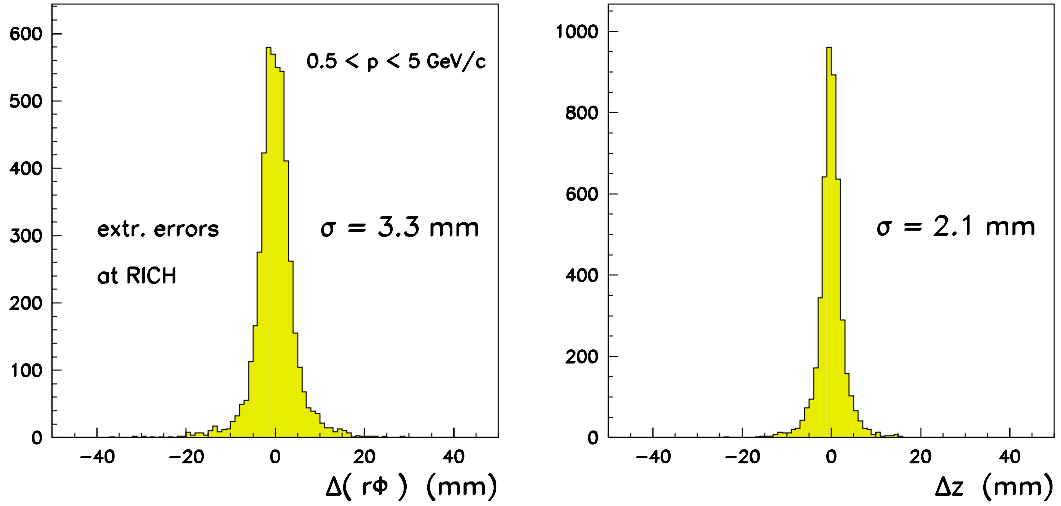


**Figure 4.24:** Distributions of difference between extrapolated and real impacts at the RICH.

**Table 4.8:** Estimated probabilities for fake matches between the track and the hit in the HMPID for a density of charged particle impacts of  $100 \text{ m}^{-2}$

Momentum range (GeV/c)	0.5–1	1–1.5	1.5–2	2–3	3–4	4–5
Fake match prob. (%)	4.6	1.4	0.8	0.4	0.3	0.2

The results show that the probability of mismatches between tracks and the corresponding hit in the HMPID is tolerable at the estimated tracking impact resolutions.

## 4.5 Optimization of the detector

In the preceding sections we have discussed the tools developed to determine and study the influence of different parameters on the performance of the HMPID in the ALICE environment together with the results obtained so far. It is important to realize that the optimization in the realistic environment is not necessarily the same as the optimization in a clean environment. For instance, the result that the resolution is better for smaller radius would not have been reached on the basis of low particle density events. The pattern recognition performed on overlapped events clearly shows the importance of the occupancy in worsening the angular resolution of the Cherenkov angle distribution and, hence, the upper momentum limit of particle identification of the HMPID.

We have reached a satisfactory resolution in a particularly hostile environment. However, we believe that further optimization of the design in some respects is still possible. This optimization would consist of decreasing all the elements that contribute to the occupancy, such as:

- reducing the material budget of the HMPID modules;
- reducing the photon feedback contribution to the noise;
- studying the possibility to use a detector gas mixture with the minimum content of hydrogen atoms;
- determining the optimum single-electron mean pulse height — a compromise between the localization accuracy, the achievable single-electron detection efficiency, and resulting Cherenkov angle resolution;
- determining the optimum size of the proximity gap for best performance in a high-occupancy environment.

These optimizations will be discussed in the following.

### 4.5.1 Optimization of the constructive elements of the detectors

The analysis of the origins of the noise hits in the HMPID shown in Table 4.4 clearly indicates that it is useful to carefully analyse any possibility to reduce the material budget of the thickest object in the module, i.e. the radiator.

As has been shown in Chapter 2, the resolution of the mean Cherenkov angle has almost no dependence on the thickness of the radiator, because the loss of emitting medium is compensated by the better resolution per photon and by the higher transparency of the thinner radiator. A decrease of  $\sim 20\%$  in the thickness seems worth studying in high-density environments.

### 4.5.2 Reduction of the photon feedback

The photon feedback effect has been described in detail in Chapter 2 and it is obvious that it contributes significantly to the overall occupancy. As an indication, the photon feedback contributes  $\sim 15\%$  of the overall occupancy in the simulated events at a HV of 2100 V. It is therefore important to achieve the lowest feedback keeping a high single-electron efficiency. Two possible ways of further improvement are: the continuation of the study of the HV dependence of the mean Cherenkov angle resolution in high-occupancy environments and the study of optimized gas mixtures that would allow for the lowest feedback and for the lowest possible hydrogen content, to lower the rate of neutron interactions in the gas.

#### 4.5.2.1 Gap size

We have started to analyse the effect of decreasing the gap length in the HMPID. However, the final decision on the exact value will depend on the optimization of two factors: the best resolution achievable and the best efficiency. A larger ring pattern means that for the particles falling in the edge region of the HMPID, i.e. when the track impact is closer to the edge than the value of the ring radius, a number of photons of the pattern will be lost because of the detector size. This problem will have to be addressed in detail and it is clear that, all other conditions being equal, one would favour a smaller ring radius. It is comforting to see that, under the present conditions of the tests and pattern recognition, the smaller size also results in the best angular resolution, as shown in Section 4.3.6.